A Critical-Strain Criterion for Hydrogen Embrittlement of Cold-Drawn, Ultrafine Pearlitic Steel

D.G. ENOS and J.R. SCULLY

A stress-modified, critical-strain model of fracture-initiation toughness has been adapted to the case of hydrogen-affected pearlite shear cracking, which is a critical event in transverse fracture of cold-drawn, pearlitic steel wire. This shear cracking occurs *via* a process of cementite lamellae failure, followed by microvoid nucleation, growth, and linkage to create shear bands that form across pearlite colonies. The key model feature is that the intrinsic resistance to shear-band cracking at a transverse notch or crack is related to the effective fracture strain at the notch root. This fracture strain decreases with the logarithm of the diffusible hydrogen concentration (C_H). Good agreement with experimental transverse fracture-initiation-toughness values was obtained when the sole adjustable parameter of the model, the critical microstructural dimension (l^*), was set to the mean dimension of shearable pearlite colonies within this steel. The effect of hydrogen was incorporated through the relationship between local effective plastic strain (ε^f_{eff}) and C_H, obtained from sharply and bluntly notched tensile specimens analyzed by finite-element analysis (FEA) to define stress and strain fields. No transition in the transverse fracture-initiation morphology was observed with increasing constraint or hydrogen concentration. Instead, shear cracking from transverse notches and precracks was enabled at lower global applied stresses when C_H increased. This shear-cracking process is assisted by absorbed and trapped hydrogen, which is rationalized to either reduce the cohesive strength of the Fe/Fe_3C interface, localize slip in ferrite lamellae so as to more readily enable shearing of Fe_3C by dislocation pileups, or assist subsequent void growth and link-up. The role of hydrogen at these sites is consistent with the detected hydrogen trapping. Large hydrogen-trap coverages at carbides can be demonstrated using trap-binding-energy analysis when hydrogen-assisted shear cracking is observed at low applied strains.

I. INTRODUCTION AND BACKGROUND

A. *Metallurgy of Isothermally Transformed Prestressing Steel*

EUTECTOID steels with a fine pearlitic microstructure are used extensively in prestressed and post-tensioned concrete structures due to their high yield strength. When utilized in such applications, these steels are candidates for cathodic protection to reduce corrosion-induced losses in the cross section, especially in marine bridge piles. Cathodic protection introduces the potential for hydrogen embrittlement of the prestressing tendon.[1,2,3] The prestressing steel investigated in this study is similar, compositionally, to AISI/SAE 1080 carbon steel, with a yield strength of 1696 MPa. The steel of interest is austenitized and isothermally transformed to a fully pearlitic condition, with an average pearlite interlamellar spacing of 95 nm. Processing of the prestressing steel involves, first, isothermally transforming the previously austenitized steel to achieve a fully pearlitic microstructure, after which it is cold drawn to an 85 pct reduction in area and stress relieved. The microstructure produced by the cold drawing of the prestressing strand is highly anisotropic, with pearlite lamellae preferentially aligned parallel to the long axis of the strand.[4,5] These wires have a $\langle 110 \rangle$ wire texture ($\langle 110 \rangle$ direction within ferrite lamellae aligned roughly parallel to the drawing axis), such that {011} planes in the ferrite are oriented at 0, 60, and 90 deg from the wire axis. Moreover, the $\langle 112 \rangle$ directions in these planes are oriented at angles of 30, 54.7, 73.2, and 90 deg from $\langle 110 \rangle$. The deformation associated with the drawing process also results in the formation of an elongated dislocation cell structure, with the cell size determined by the combination of the interlamellar spacing of the pearlite coupled with the degree of cold work.[4] The interlamellar spacing within the pearlite and fine dislocation cell structure controls the yield strength of both isotropic and anisotropic eutectoid steels. Ductility is controlled by the lamellar spacing, pearlite colony size, carbide thickness, and prior-austenite grain size. The role of hydrogen in each of the controlling processes is not well understood. Typical fracture-initiating inclusions in such steel include MnS, Ti(C,S), and Al-Ca-S.[6,7,8]

B. *Fracture Toughness of Isothermally Transformed Prestressing Steel*

Due to the highly anisotropic nature of the pearlite, the limited ferrite slip distance, more homogeneous slip, and the ability of fine cementite to deform in response to tensile deformation,[6,9] prestressing steels possess a high transverse mode I (*i.e.*, crack perpendicular to the wire axis) fracture toughness when tested in laboratory air, with values as high as 80 MPa-m$^{1/2}$ reported in the literature.[10] However, the longitudinal fracture toughness is typically very low, with values of 10 to 25 MPa-m$^{1/2}$ cited in the literature.[11,12] In the uncharged state, fracture of an isotropic fully pearlitic steel (*i.e.*, pearlite colonies randomly oriented throughout the microstructure) consists predominantly of two modes.

D.G. ENOS, Scientist, is with the 3M Austin Center, Austin, TX 78726-9006. J.R. SCULLY, Professor of Materials Science and Engineering, is with the Center for Electrochemical Science and Engineering, Department of Materials Science and Engineering, University of Virginia, Charlottesville, VA 22903-2442. Contact e-mail: jrs8d@virginia.edu

Manuscript submitted November 9, 2000.

The first, known as the "shear-cracking process" proposed by Miller and Smith,[13] consists of the formation of slip bands within the ferrite lamellae in pearlite colonies oriented such that the lamellae are parallel to the tensile axis.[7,8,13–15] The resulting stress concentration caused by the slip bands results in fracture of the individual cementite lamellae. The failed cementite lamellae subsequently provide an easy path for further local deformation. As a result, more intense shear occurs within the ferrite lamellae, which causes additional cementite lamellae to fail. With increased deformation, the initial voids which resulted from the fractured cementite lamellae become large and link up, resulting in a macroscopic crack. This form of cracking will occur along the plane of maximum global shear stress, approximately 45 deg from the tensile axis within an isotropic material, within appropriately aligned pearlite colonies. A second type of fracture mode is transgranular cleavage, occurring on {100} planes within the ferrite, with cleavage facets confined to one or more closely oriented pearlite colonies.[14] Cleavage has been demonstrated to occur across several adjacent pearlite colonies whose ferrite lamellae share a common {100} orientation.[14,15] Such cleavage occurs at the peak-stress location ahead of a transverse notch or sharp crack and is oriented 90 deg from a tensile axis (*i.e.*, mode I).[15] Nucleation sites are believed to be either microcracks associated with MnS inclusions previously fractured during processing, or other cracks associated with pearlite colonies, such as the shear cracking discussed previously. In general, cleavage is found to be more prevalent in notched and precracked specimens with high tensile-stress triaxiality, where it has been observed to overtake or interrupt the microvoid coalescence (MVC) process associated with shearing across pearlite colonies. Such cleavage is in contrast to the almost exclusively ductile MVC typically observed in unnotched tensile specimens. In drawn eutectoid steels, the cleavage cracking common in isotropic pearlite is actually reduced. Instead, ductile void nucleation, growth, and coalescence may be interrupted by brittle cracking at 70 to 90 deg from a transverse notch or precrack oriented perpendicular to the drawing axis.[16] This form of cracking is known as "longitudinal splitting." Longitudinal splitting is best characterized as brittle, cleavage-like cracks propagating parallel to the pearlite lamellae and, consequently, to the drawing axis of the steel wire. The fracture toughness associated with this mode is low, as discussed previously.

C. *Hydrogen Embrittlement of Isothermally Transformed Prestressing Steel*

High-strength, low-alloy steels of similar yield strength have been demonstrated to be severely embrittled by hydrogen, with a mode I fracture toughness on the order of 20 MPa-m$^{1/2}$.[17] However, cold-drawn pearlitic steels stressed along the wire axis, whether stress relieved or not, are highly resistant to hydrogen embrittlement when compared to quenched and tempered low-alloy steels.[18] The increased resistance to hydrogen embrittlement from transverse notches or cracks has been postulated to be the result of the highly anisotropic microstructure (*i.e.*, pearlite lamellae preferentially aligned parallel to the tensile axis are perpendicular to the crack front of an advancing mode I crack from a transverse notch or flaw). Moreover, weakened interfaces, such as elongated prior-austenite grain boundaries and dislocation cell boundaries parallel to the wire axis, cannot be readily subjected to high mode I loading. Aligned pearlite has the effect of diverting a propagating mode I crack parallel to the drawing axis, much like a lamellar composite, where the applied-stress intensity is considerably lower. When eutectoid steels with isotropic pearlitic microstructures are hydrogen charged, the predominant failure mode has been found to become a locally ductile, tearing-topography surface (TTS),[19] as demonstrated by Toribio *et al*.[20,21,22] The TTS is a nonclassical fracture mode observed in a number of alloy systems and appears to be the result of ductile or microplastic tearing on a submicron scale.[23] The location of fracture initiation in this case is unclear. It has been suggested that crack initiation occurs at the location of the maximum stress or strain,[19,22] at some combination of the two,[19] or when a critical stress or strain is exceeded over some microstructurally significant distance.[7,19] Ferrite-pearlite boundaries, nonmetallic inclusions (*e.g.*, MnS), and pre-existing cementite microcracks within the pearlite have all been suggested as initiation sites.[23]

Unfortunately, while some research has been completed on the mechanisms of crack initiation and growth both with and without hydrogen for isotropic pearlitic microstructures (*i.e.*, randomly oriented pearlite colonies), work done on heavily cold-worked microstructures such as that present in the prestressing steel, while extensive,[16,24–26] has not isolated the events that promote cracking from transverse notches or catastrophic longitudinal splitting. Studies on hydrogen-charged, cold-worked pearlitic steel wires have revealed several common features. Experiments[27] on fine pearlitic (interlamellar spacing not specified), cold-drawn 1075 bend bars (σ_{YS} = 1461 MPa and σ_{UTS} = 1682 MPa) hydrogen charged in H_2S lead to the observance of cracking 45 deg to the wire axis, which was attributed to the texture of the wire. Experiments[26] conducted on hydrogen-charged AISI 4140 wire bend bars (austenitized, quenched, tempered, and drawn) also found cracking to occur at 45 deg from the tensile axis. In addition, increased hydrogen charging (300 to 38,800 μA/cm^2 in 1 N H_2SO_4 + 1 g/L thiourea) increased the amount of longitudinal splitting, parallel to the tensile axis. The longitudinal splitting was assumed to occur along the dislocation cell boundaries discussed previously. Experimentation conducted on smooth prestressing steel (σ_{YS} = 1590 MPa and σ_{UTS} = 1800 MPa) tensile bars[28,29] has revealed fracture surfaces dominated by ductile shear and longitudinal splitting. Nucleation was assumed to occur at fractured nonmetallic inclusions (presumably MnS) within the steel, but fractographic evidence was not presented in either study. Based on the fractography from the former studies, some of the fracture surfaces may be described as TTS. Experimentation on notched and precracked samples of a prestressing tendon compositionally similar to AISI/SAE 1085[1] revealed four distinct fracture regions: (1) ductile (MVC) regions perpendicular to the tensile axis, (2) regions of cleavage surrounded by ductile regions, (3) longitudinal splitting, and (4) shear lips along the peripheral regions of the sample, although the nucleation site was not identified. Moreover, no effort was made to quantify the exact diffusible hydrogen concentrations in any of the aforementioned studies.

Experiments on precracked prestressing steel tendons[16] both in charged and uncharged states revealed crack propagation that progressed at an angle 70 to 90 deg from the plane of the transverse precrack, turning roughly parallel to the tensile axis. This behavior was in stark contrast to the hot-rolled material of the same composition, where TTS was observed when uncharged, but cleavage was observed upon charging to -1.2 V_{SCE} within a $Ca(OH)_2$ solution. The hot-rolled material also exhibited consistently lower failure loads at a given E_{app}. In the transition region for the cold-drawn material (*i.e.*, the transition from a fatigue precrack to a hydrogen crack) near the transverse fatigue precrack, the fracture mode was predominantly microvoid coalescence with small cleavage facets and some longitudinal splitting. In the case of the cathodically charged samples, although there was a reduction in the fracture load relative to the fracture load in air, there was no change in the fracture mode or length scale of the features within the fracture surface. Neither the hydrogen concentrations (the governing microstructural feature that triggered longitudinal splitting) nor the fracture initiation site were determined.

At present, the mechanism of hydrogen-assisted fracture initiation from transverse flaws of the drawn, fully pearlitic prestressing strand is unclear. In isotropic pearlitic structures (*i.e.*, randomly oriented pearlite colonies), the fracture mode in the uncharged case is predominantly cleavage in specimen geometries which promote a large degree of tensile-stress triaxiality.[20,21] When such specimens are hydrogen charged, the failure mode becomes predominantly ductile in nature (*i.e.*, TTS failure). Conversely, in the case of drawn pearlitic wire, the failure mode appears to be predominantly ductile shear in both the charged and uncharged case, with no significant change in the microscopic fracture-initiation mode as the hydrogen concentration is increased. There is also a large amount of subsequent longitudinal splitting (*i.e.*, crack propagation parallel to the tensile axis) in cold-drawn pearlitic steels, both when charged and uncharged. The degree of longitudinal splitting has been observed to increase with charging severity, although the exact hydrogen concentrations have not been quantified. This difference in behavior between the drawn and undrawn material is likely the result of the highly anisotropic nature of the pearlite lamellae within the drawn material, coupled with the existence of a cellular dislocation structure within the ferrite lamellae. What triggers the catastrophic transition to longitudinal splitting, analogous to the catastrophic transition to cleavage in isotropic euctectoid steels, is currently unknown.

This study seeks to advance the understanding of the effect of diffusible and trapped hydrogen on the development of shear cracks from transverse notches and cracks, which may, in turn, lead to either cleavage or longitudinal splitting. Studies were conducted on bluntly notched, sharply notched, and fatigue-precracked specimens, as a function of a preselected range of diffusible hydrogen concentrations. The authors are unaware of any study that provides a direct correlation between the diffusible (far-field) and/or local (trapped) hydrogen concentrations and the tendency for shear-crack formation in this type of steel. Based upon the literature, it is reasonable to hypothesize that one possible event leading to catastrophic cleavage or longitudinal splitting is either wholesale shear cracking across pearlite colonies or microcracking at inclusions, either of which, in turn, provide the critical flaw for subsequent catastrophic failure

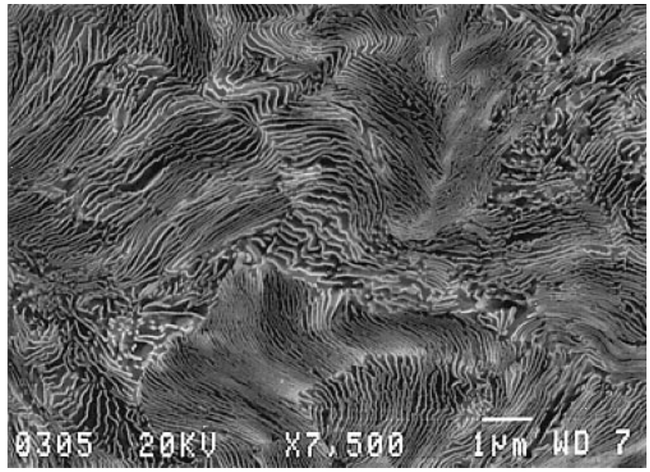

Fig. 1—High-magnification view (parallel to the drawing axis) of the drawn, fully pearlitic microstructure in isothermally transformed ASTM A416 grade 270 prestressing steel strand.

(*e.g.*, by cleavage or splitting). We seek to characterize such behavior and develop a model to better explain hydrogen embrittlement initiation.

II. EXPERIMENTAL

A. *Materials*

An ASTM A416 grade 270 low-relaxation prestressing strand was obtained from Florida Wire and Cable, Inc., Jacksonville, FL. The prestressing tendon possessed a nominally fully pearlitic microstructure (95 nm interlamellar spacing), as illustrated from a point of view parallel to the drawing axis in Figure 1. The microstructure was composed of a distribution of small pearlite colonies, ranging in size from 2 to 10 μm. These colonies are likely the result of the drawing process, which has been demonstrated to transform initially uniform grains into elongated, ribbon-like grains which curl about the drawing axis in cold-drawn, bcc [011] textured materials.[30] There was no evidence of the existence of prior-austenite grain boundaries, nor of the presence of proeutectoid phases (ferrite or cementite) or other large-scale microstructural features. As is typical with steels of this composition, there were a large number of inclusions throughout the microstructure.[6] The average spacing between MnS inclusions was found to be approximately 20 μm. These inclusions were elongated parallel to the drawing axis due to the drawing process, with the aforementioned spacing being measured in a plane perpendicular to the drawing axis. The drawing process has a rather dramatic effect on the microstructure of the strand. The microstructure produced by the cold drawing of the prestressing strand is highly anisotropic, with pearlite lamellae preferentially aligned parallel to the tensile axis,[4,5] and contains shear bands and microvoids within the microstructure.[6] The wire has been found to have a $\langle 110 \rangle$ texture (with respect to ferrite lamellae), such that $\{100\}$ planes within the ferrite are preferentially oriented 45 deg to the wire axis. A dislocation cell size on the order of 35 nm is expected. Due to the ultrafine pearlitic microstructure coupled with the large amount of cold work experienced by the prestressing strand, very high strength ($\sigma_y > 1400$ MPa) is achieved. The 0.2 pct offset

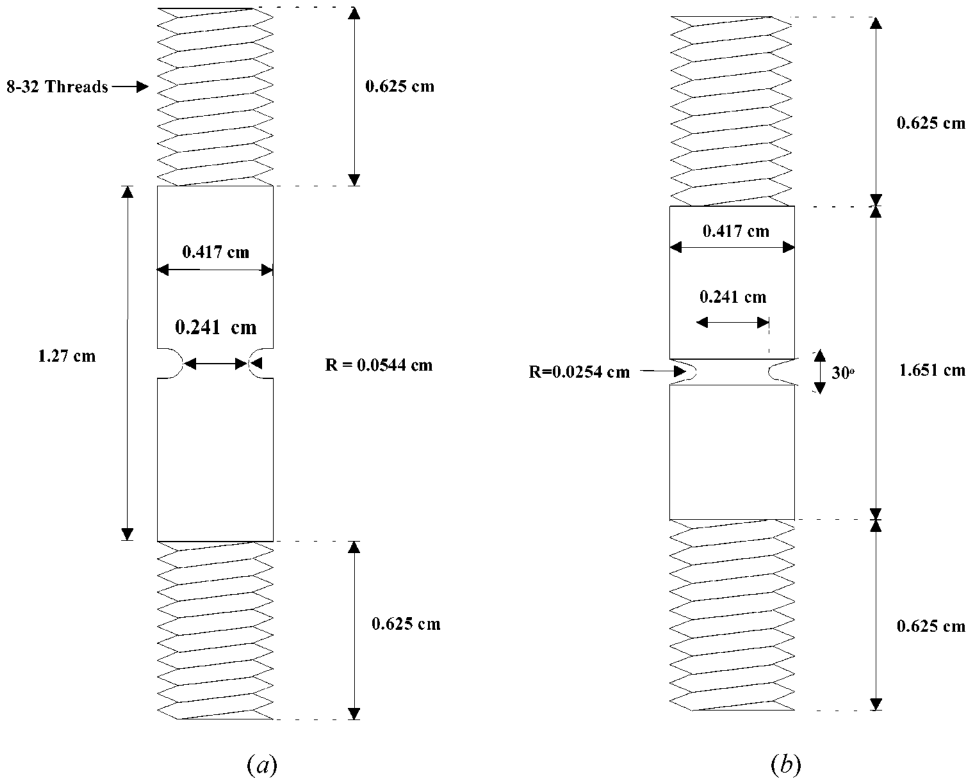

Fig. 2—Circumferentially notched tensile bars utilized to perform constant extension rate experiments using individual prestressing steel tendo ns. Samples with a plastic constraint value of (*a*) 1.08 and (*b*) 1.27 are illustrated.

yield strength was 1696 MPa, and the elastic modulus was 185 GPa, in agreement with literature values for drawn pearlitic wire.[10,15,24,27,31–35]

B. *Determination of the Fracture-Initiation Stress for Notched Tensile Bars*

Constant-extension-rate tensile (CERT) tests were performed on circumferentially notched tensile bars with an as-machined (32 rms) surface finish and triaxial stress-constraint factors (cf) of 1.08 and 1.50 to define the local stresses and strains at crack initiation (Figure 2).* Tensile bars were machined such that the tensile axis of the bar was parallel to the drawing axis of the prestressing tendon. Samples were degreased ultrasonically in methanol and the dimensions were documented. Several experiments were performed on uncharged notched, as well as smooth, tensile bars in air, to establish the baseline tensile strength and plastic-flow properties of the steel. The CERT testing was then performed at a series of potentiostatically applied cathodic potentials in various environments. A set of permeation experiments was also conducted over the same range of potentials to obtain the relationship between C_H and the applied potential.** These relationships were utilized to define C_H for each fracture-initiation test and have been reported elsewhere.[36–39] All CERT tests were performed at a crosshead displacement rate of 1.71×10^{-8} m/s, a rate demonstrated to maximize the hydrogen embrittlement effects for a prestressing strand as observed by Hartt *et al.*[2] and Toribio *et al*.[20,21] Precharging prior to CERT ensured a uniform hydrogen concentration, as discussed elsewhere.[36] The output from this testing was the remote breaking load and C_H for blunt and sharp specimens.

Stress and strain distributions within the notched tensile bars were assessed *via* finite-element analysis (FEA) at various applied remote-section stresses. The ABAQUS* software was used to conduct an elastic-plastic analysis at various remotely applied loads, from which the relevant local stress and strain distributions were obtained, utilizing global yield- and flow-property data from smooth tensile bars (*i.e.*, a true stress–true strain curve). Symmetry was exploited to construct an FEA mesh (20 μm) from the specimen centerline to the notch surface, as discussed elsewhere.[40] The local longitudinal, radial, and circumferential stress and strains were obtained as a function of position in front of the notch from FEA, in the equatorial plane normal to the notch root.** A higher shear stress and effective plas-

*The cf value is defined as the ratio of the mean to effective stress within the notch (*i.e.*, cf = $\sigma_{mean}/\sigma_{eff}$); as a point of reference, the cf value for a sharp crack is 2.50 and that for an un-notched sample is 0.33.

**C_H is the diffusible hydrogen concentration, composed of hydrogen present in lattice-interstitial sites and reversible traps (*i.e.*, trap sites with binding energies approaching kT at room temperature). The total hydrogen concentration, equal to the sum of the mobile and irreversibly trapped hydrogen, is several times greater than C_H.

*ABAQUS is a trademark of Hibbitt, Karlsson, & Sorenson, Inc., Pawtucket, R.I.

**By varying the fineness of the mesh used for the FEA, it was possible to positively identify the location of the position of maximum stress/strain, eliminating errors that would arise from an overly coarse mesh. It should be noted that this analysis assumes that global stress-strain properties can be applied to each mesh element and does not account for microstructural-scale anisotropy in the material.

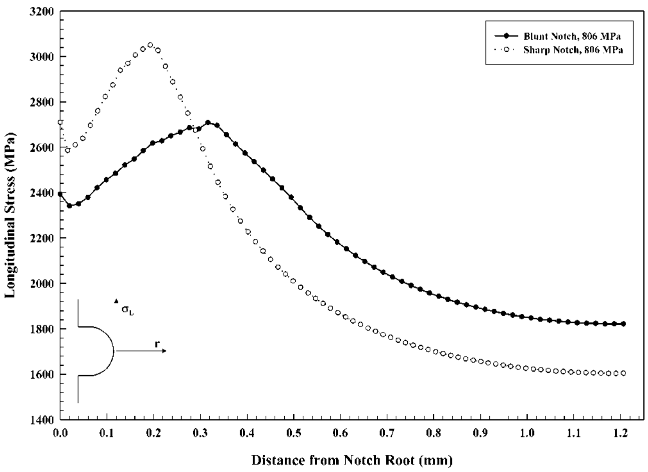

Fig. 3—Longitudinal stress distribution (from FEA) along equator of the notch root as a function of notch geometry for a fixed remote stress, illustrating the larger radial depth of elevated stress for the blunt notch.

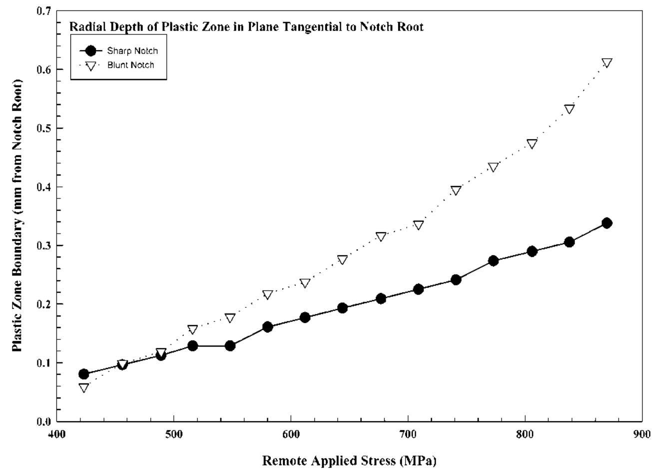

Fig. 4—Radial depth of the plastic zone along equatorial position of the notch as a function of the remotely applied load for the blunt and sharp circumferentially notched tensile specimens.

tic strain is achieved at the specimen surface relative to the radial distance along the equator, in the case of both the sharply and bluntly notched specimens. The depth of the region where the shear stress and effective strain are enhanced is larger for the blunt notch. A higher peak-stress level was achieved for the sharp notch, but the radial dimension over which the stress was elevated was smaller. The region of elevated stress is much broader at a given remote applied stress for the blunt notch. Moreover, the position of the maximum longitudinal stress was a greater distance from the notch root for the bluntly notched sample at a given remote stress. These effects are demonstrated in Figure 3.

The FEA analysis, in conjunction with fractographic analysis of the initiation location, was used to determine whether crack initiation occurred at the position of peak hydrostatic stress (*e.g.*, stress control) or at the location of peak strain (*e.g.*, strain-controlled initiation). It is notable that Lewandowski observed a crack-initiation location in an isotropic, pearlitic eutectoid steel closer to the notch surface than the location of peak stress, suggesting the joint requirement for a critical strain and tensile stress to initiate cracks in a pearlitic steel.[15] Moreover, the size (radial depth in from the notch root) of the plastic zone in the plane of the notch is greater for the bluntly notched specimen at a given applied remote stress (Figure 4). As a result, assuming that crack initiation occurs at some microstructurally significant region within the plastic zone, the effective at-risk volume is greater for the blunt notch than the sharp one.

To verify that breaking loads were close to crack-initiation loads, a number of CERT experiments were performed on doubly notched tensile specimens (using both notch acuities). In these experiments, as well as in experiments where the test was halted close to, but preceding, failure of the tensile bar, metallographic sectioning was performed to detect cracks. Serial sectioning verified the existence of minimal subcritical cracking beneath the notch at loads below the breaking load. This is likely the result of the fine pearlitic microstructure of the prestressing strand. A similar nonresult was obtained by Kavishe and Baker[31] utilizing notched bend bars. Although documentation of subcritical cracking beneath the notch in coarse pearlitic microstructures was enabled, microstructures with an increasingly fine

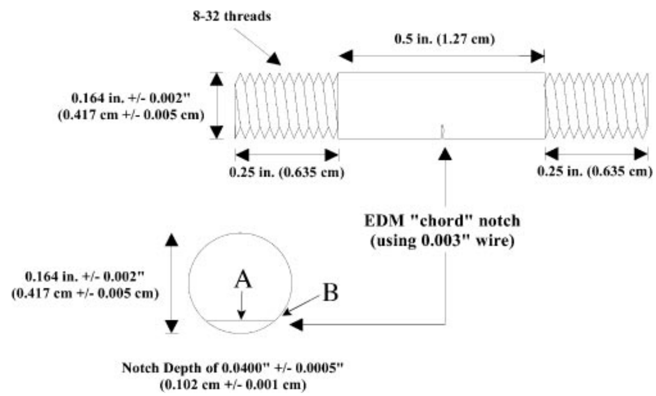

Fig. 5—Prestressing steel tendon with transverse EDM chord notch utilized for small crack fracture mechanics experiments to determine transverse fracture toughness.

interlamellar spacing did not exhibit any subcritical cracking beneath the notch root.

C. *Determination of the Threshold-Stress Intensity for Crack Initiation From Transverse Precracks*

Determination of the transverse K_{IHE} was accomplished *via* experiments performed on transverse fatigue-precracked specimens. These experiments also served to assess the effect of further reducing the at-risk volume by reducing the plastic-zone size for a given applied remote stress and raising the local tensile stress to 3 to 5 times the yield strength. Chord-notched tensile bars (Figure 5) were produced by electrodischarge machining (EDM) a transverse chord notch perpendicular to the wire axis with a root radius of 4 mils (0.0102 cm). Each sample was fatigue precracked to achieve a precrack perpendicular to the wire axis under load control, utilizing an Instron servohydraulic system. A 10 Hz sinusoidal waveform with a peak-to-peak amplitude of 1 kip (4448 N) was applied. An initial offset of 50 lbs (222 N) was utilized to prevent compression of the sample during precracking. Precracks were semicircular in nature, with a depth of 0.5 mm at the crack center (corresponding to a 90 μV change in the direct current potential drop (DCPD) crack potential). The crack-initiation toughness was determined by monitoring the DCPD signal while applying progressively increasing load steps. The load was first ramped from a preload of 400 lbs (1780 N) to an initial load of 500 lbs (2224 N). The load was then progressively increased in 100-lb increments until crack initiation occurred. Each load increase was in the form of a ramp over 5 minutes. Each load was held for sufficient time to allow stress-assisted, diffusive redistribution of hydrogen in front of the crack tip. It was assumed that the hydrogen had to diffuse a distance equivalent to the position of the maximum hydrostatic stress in front of the sharp notch, or approximately 0.2 mm, based on the FEA data reported previously. Using typical saturation curves and the effective diffusivity of hydrogen in the prestressing steel (6.72×10^{-7} cm^2/s, as previously determined[37]), this results in an average time of 3 minutes and 10 seconds. As a result, each load was held for a period of 30 minutes (approximately 10 times the theoretical time required for hydrogen redistribution), after which it was increased to the next level.

Experiments were performed in a saturated $Ca(OH)_2$ environment, for which permeation data were available.[37,39] The solution was stirred *via* a recirculation system. Experiments were conducted in the uncharged state, as well as at a steady-state C_H of 5×10^{-7}, 2×10^{-6}, and 2×10^{-5} mol H/cm^3 (0.064, 0.254, and 2.54 wppm, respectively). All hydrogen-charged samples were precharged for 12 hours prior to testing, allowing the establishment of a uniform hydrogen concentration throughout the test sample. The same charging potential used to precharge the sample was then applied throughout the duration of the experiment. Thus, the electrochemical and environmental conditions were controlled such that (1) the applied potentials were highly cathodic in nature, and (2) the environment (saturated $Ca(OH)_2$) was buffered against substantial pH changes. The combination of the aforementioned conditions ensured that the diffusible hydrogen concentration in front of the notch was equivalent to the global diffusible hydrogen concentration, C_H.

Numerous solutions exist for the stress intensity for elliptical- and straight-fronted transverse cracks within cylindrical tension samples. Analyses are performed at two locations along the crack front, as illustrated in Figure 5: at the center of the crack (location A) and at the intersection of the edge of the crack front with the edge of the specimen (location B). FEA[10,41–47] is typically used to calculate the boundary correction factor used to address the nature of the crack. These relationships are of the general form[46]

$$K_{IC} = \sigma_i F \sqrt{\pi a} \qquad [1]$$

where σ_i is the remote applied stress, a is the crack length, F is the boundary correction factor, and K_{IC} is the transverse fracture toughness. For a semicircular crack front, the maximum stress intensity is achieved at location B, at the surface. Tables were used to estimate K_I as a function of position along the crack front. The solution of Raju and Newman[47] was used for an elliptically fronted crack:

$$K_I = \left(\sigma_i \sqrt{\pi \frac{a}{Q}}\right) F \qquad [2]$$

where σ_i is the remotely applied stress, a is the maximum crack depth, Q is a shape factor accounting for the elliptical crack front (Reference 47 provides appropriate expressions), and F is a boundary correction factor (tabulated in Reference 47), again, accounting for the geometry of the crack front.

For a typical crack length of 1.7 mm, $K_{Applied}$ must be less than or equal to 45 MPa-m$^{1/2}$ to be a valid determination of K_{IC} using the ASTM E399 and ASTM E1681 criteria. However, considering the microstructure of the prestressing tendon (*i.e.*, alternating lamellae of ferrite and cementite), the deforming phase (*i.e.*, ferrite) is observed to be highly constrained by the cementite lamellae, behaving much like a metal-matrix composite. There will be little, if any, difference in the obtained stress intensity as a function of the level of constraint determined by the geometry of the test specimen, since a much higher level of constraint is imposed by the microstructure than could be achieved by specimen geometry. The determined K_{IC} value is insensitive to specimen thickness, as has been found for metal-matrix composites.[48] Thus, valid K_{IC} results may be achieved for values of K_Q as high as 90 MPa-m$^{1/2}$.

D. *Quantification of Diffusible and Trapped Hydrogen Concentrations*

Hydrogen permeation experiments were used to obtain the diffusible hydrogen concentrations and effective diffusivity. The procedures used to determine C_H and D_{eff} are extensively covered elsewhere.[36–39,49–52] Thermal desorption spectroscopy (TDS) was utilized to assess hydrogen trapping and partitioning within the prestressing steel.[53–58] In short, precharged steel cylinders were held at room temperature to outgas lattice hydrogen. Heating rates of 2.5 °C/min, 5.1 °C/min, 7.6 °C/min and 10.3 °C/min were used to conduct desorption experiments and determine the temperatures associated with desorption peaks for each trap state. From the literature, the expression

$$\frac{\partial\left(\ln\left(\frac{\phi}{T_{max}^2}\right)\right)}{\partial\left(\frac{1}{T_{max}}\right)} = -\frac{(E_b + E_m)}{\mathrm{R}} \qquad [3]$$

has been derived,[53] where φ is the thermal ramp rate, T_{max} is the temperature at maximum desorption, E_b is the trap-site binding energy, E_m is the migration energy, and R is the gas constant. Thus, a plot of ln (φ/T_{max}^2) *vs* $1/T_{max}$ will be linear, with a slope of $-(E_b + E_m)/\mathrm{R}$. Prior to performing each TDS experiment, sufficient time at 25 °C was allowed for the diffusible hydrogen to completely diffuse out of the sample. As such, each peak observed within a TDS spectra corresponds to a specific trap site within the steel and not to diffusible or weakly trapped hydrogen.

The trap-site coverage predicted for a given lattice coverage (θ_L) may be calculated utilizing the binding energies determined above *via* the expression

$$\left(\frac{\theta_T}{1-\theta_T}\right) = \left(\frac{\theta_L}{1-\theta_L}\right)\exp\left(\frac{E_b}{\mathrm{R}T}\right) \qquad [4]$$

where θ_T and θ_L represent the trap-site and lattice-hydrogen coverages, respectively. The value of θ_L associated with each charging condition was determined from C_L/N_L, where C_L is the lattice-hydrogen concentration associated with interstitial sites and N_L is the density of interstitial sites in bcc iron. The value of C_L was determined from the same steady-state

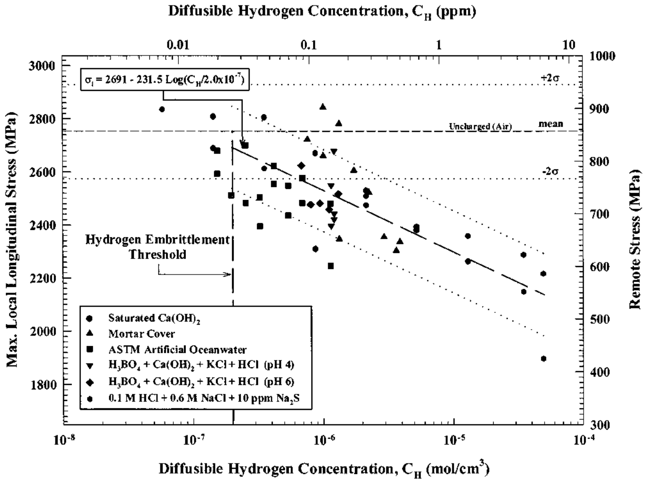

Fig. 6—Universal curve expressing the local maximum and equivalent remote fracture stress of the notched eutectoid prestressing steel as a function of C_H for the bluntly notched tensile specimens in all environments.

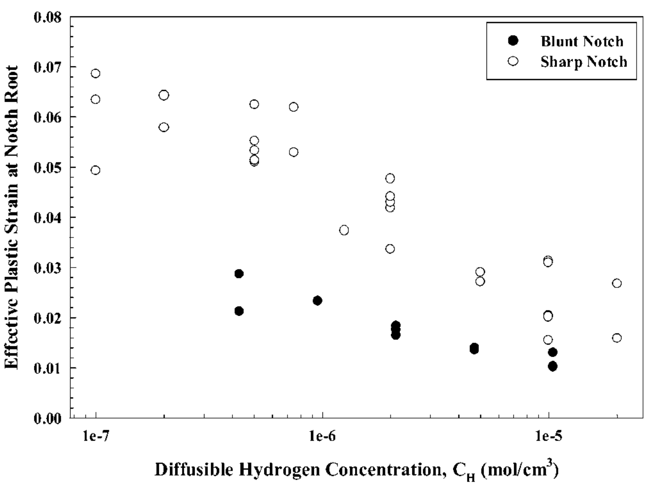

Fig. 7—Effective plastic strain at the position of the notch roots *vs* C_H for notched eutectoid prestressing steel. Effective plastic strain was obtained from FEA at the remote stress associated with fracture initiation.

permeation data used to determine C_H, with the exception that a tortuosity factor multiplied by the perfect lattice diffusivity D_L was used to determine C_L from the steady-state hydrogen flux and known sample thickness. A tortuosity factor of 0.2 was used to account for the path through the bcc iron phase.

III. RESULTS

A. *Hydrogen Embrittlement of the Drawn, Pearlitic Wire Utilized as Prestressing Steel*

1. *Transverse fracture initiation from a bluntly notched tensile bar*

Bluntly notched tensile bars exhibited a remote breaking stress that decreased monotonically with log (C_H). Figure 6 presents a summary of the applied remote stress and corresponding maximum longitudinal stress as a function of C_H for CERT experiments conducted in a variety of environments. Similarly, Figure 7 presents the effective plastic strain at failure *vs* C_H. The threshold diffusible hydrogen concentration (C_{Hcrit}) required to produce embrittlement can also be obtained from the plot and is found to be approximately 2×10^{-7} mol/cm^3 (0.0254 wt ppm). An empirical relationship was found between the maximum longitudinal stress and C_H:

$$\sigma_F \text{ (MPa)} = 2691 \pm 155 - 231.5 \log\left(\frac{C_H}{2.0 \times 10^{-7}}\right) \quad [5]$$

A similar expression was found for the effective plastic strain (ε_{eff}), here taken at the notch-surface equatorial position from FEA:

$$\varepsilon^f_{eff} = 0.029 - 0.01 \log\left(\frac{C_H}{2.0 \times 10^{-7}}\right) \quad [6]$$

Since all data fit within a single band, it is clear that the degree of embrittlement of the prestressing tendon for a given hydrogen concentration is a function only of log (C_H) and is independent of the environment in which the test was performed. Other researchers have arrived at similar conclusions for hydrogen-embrittled steels.[17,59]

Similar relationships may also be derived *via* the previously discussed FEA results to express both the achieved plastic-zone size at the crack-initiation stress (r_p) and the radial position of maximum hydrostatic stress as a function of the steady-state C_H. These relationships are found to be

$$r_p \text{ (mm)} = 0.491 - 0.133 \log\left(\frac{C_H}{2.0 \times 10^{-7}}\right) \quad [7]$$

$$\text{Depth of maximum Hydrostatic Stress (mm)} = 0.328 - 0.085 \log\left(\frac{C_H}{2.0 \times 10^{-7}}\right) \quad [8]$$

where r_p is the radial depth of the plastic zone along the notch equator in millimeters, and C_H is the steady-state diffusible hydrogen concentration (lattice + weakly trapped) in mol/cm^3. Even at the highest hydrogen concentrations, which resulted in the lowest breaking loads, the steel experienced plastic deformation near the notch root, with a depth of 50 μm along the notch equator at the lowest remote breaking stresses. The plastic zone is expected to be greater in depth at an angle of 45 deg from the notch equator. The size of the plastic zone (as well as the corresponding positions of maximum longitudinal and hydrostatic stress) was large relative to the pearlite colony size (2 to 10 μm) and inclusion spacing (20 μm), even at high C_H levels.

2. *Transverse fracture initiation from a sharply notched tensile bar*

The fracture-initiation stress as a function of C_H is presented in Figure 8. It can be seen in the figure that the sharp notch has much less scatter than the blunt notch. It is possible to extract both C_{Hcrit} as well as a relationship between C_H and the fracture-initiation stress, as for the bluntly notched tensile bars. The value of C_{Hcrit} was found to be 3.25×10^{-7} mol/cm^3 (0.0413 ppm). The empirical relationship established between the maximum longitudinal fracture-initiation stress and C_H was

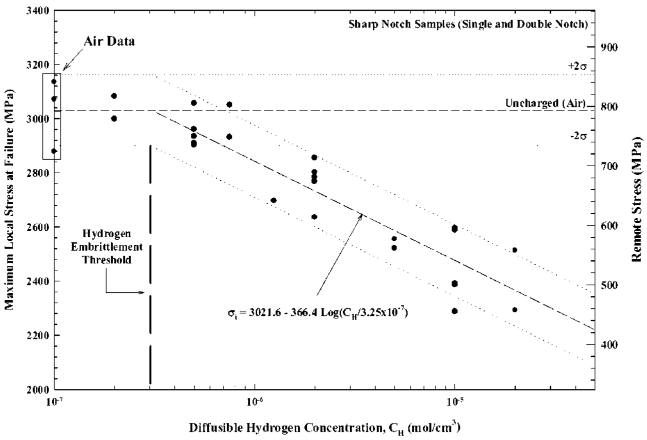

Fig. 8—Remote stress and local maximum fracture initiation stress from FEA as a function of C_H for sharply notched eutectoid prestressing steel. All tests were performed in saturated $Ca(OH)_2$.

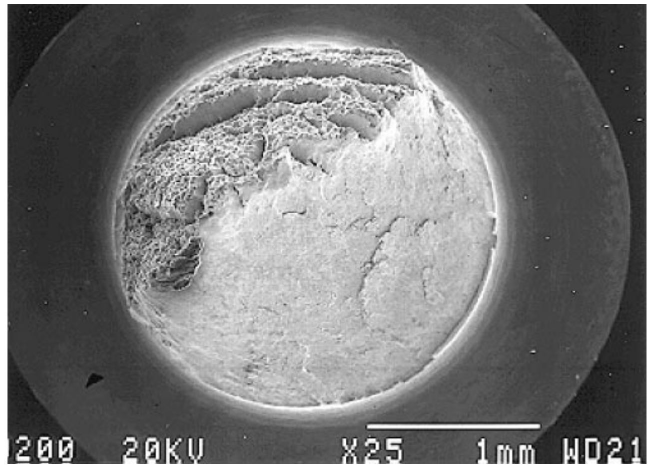

Fig. 9—Overview of the fracture surface for an uncharged, sharply notched ASTM A416 isothermally transformed prestressing steel tendon after fracture in tension.

$$\sigma_F \text{ (MPa)} = 3021.6 \pm 132 - 366.4 \log \left(\frac{C_H}{3.25 \times 10^{-7}} \right) \quad [9]$$

where 3021.6 MPa is the maximum longitudinal stress in air, σ_{air}. The value of σ_{air} is elevated over that of the bluntly notched tensile bars, and σ_F declines more rapidly with increasing C_H. Similarly, the maximum effective plastic strain at failure, taken from FEA at the notch surface, was

$$\varepsilon^f_{eff} = 0.056 - 0.02 \log \left(\frac{C_H}{3.25 \times 10^{-7}} \right) \quad [10]$$

Relationships similar to those derived for the blunt notch may also be derived to express the plastic-zone size at failure (r_p) and the depth of the maximum hydrostatic tension as a function of C_H. As with the blunt notch, both the plastic-zone depth and the depth of the maximum hydrostatic tension were large relative to the size of all microstructurally significant features (*i.e.*, pearlite colony and inclusion spacing).

3. *Fractography for bluntly and sharply notched tensile bars: Low* C_H *levels*

The notched tensile bars (*i.e.*, bluntly and sharply notched) exhibited nominally identical behavior in terms of both the macroscopic and microscopic features of the fracture surface when tested in air. Figure 9 presents the typical fracture surface representative of the as-received and low-C_H tests. There are three distinct macroscopic regions of the fracture surface. The first is a large tortuous region oriented at a large angle (approximately 70 deg) to the tensile axis. This tortuous region is terraced in nature, the result of longitudinal splitting, which is brittle in nature. These terraces are linked together by ductile and, in some cases, brittle (*i.e.*, cleavage) plateau regions. The size of the ledge and terrace regions is similar to the pearlite colony size (*i.e.*, on the order of 10 to 20 μm). The second fracture region is located at the edge of the fracture surface along portions of the circumference of the tensile bar at the notch root (predominantly at the edge of the tortuous region) and is oriented at an angle roughly 45 deg from the tensile axis and, hence, 45 deg from the equatorial position of the notch (Figure 10). This region contains many small areas which are composed of

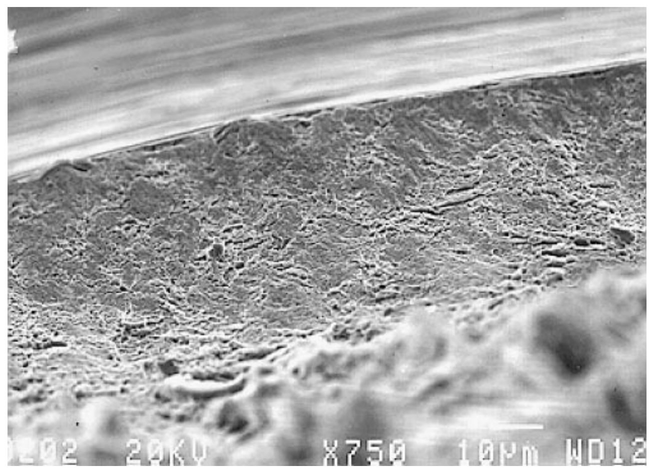

Fig. 10—Lip region around portions of the periphery of the fracture surface for an uncharged, prestressing steel tendon machined into a circumferentially notched tensile bar. The notch root is seen at the top.

numerous lamellar voids 90 to 140 nm in width, which is roughly equivalent to the interlamellar spacing of the pearlite (95 nm), presented previously (Figure 11). These latter regions are likely the result of the tensile shear-cracking process proposed by Miller and Smith,[13] as will be discussed in detail subsequently.

4. *Moderate* C_H *levels*

As C_H was increased above C_{Hcrit}, there was little change in fractography. The only pronounced change was observed within the microscopically ductile edge region (around portions of the circumference of the tensile-bar notch, particularly along the edge of the tortuous region). Many more of the lamellar void regions (as presented previously for the lower C_H levels) are evident at this C_H level, as compared to the lower C_H levels or the uncharged case, although the dimensions of the actual voids are unchanged (Figure 12).

5. *High* C_H *levels*

At a C_H of 2×10^{-5} mol/cm^3, the large, macroscopically smooth, shear-overload region oriented at 45 deg to the tensile axis has largely vanished, although numerous smaller

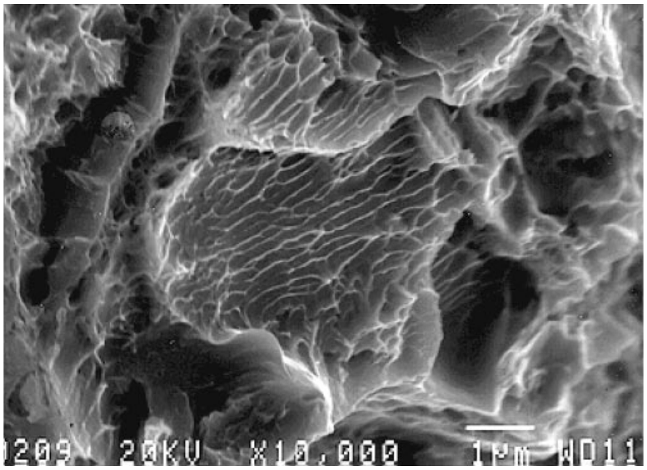

Fig. 11—Ductile region of pearlite shearing within the lip pictured above consisting of an array of lamellar voids, likely the result of shear cracking, as proposed by Miller and Smith.[13]

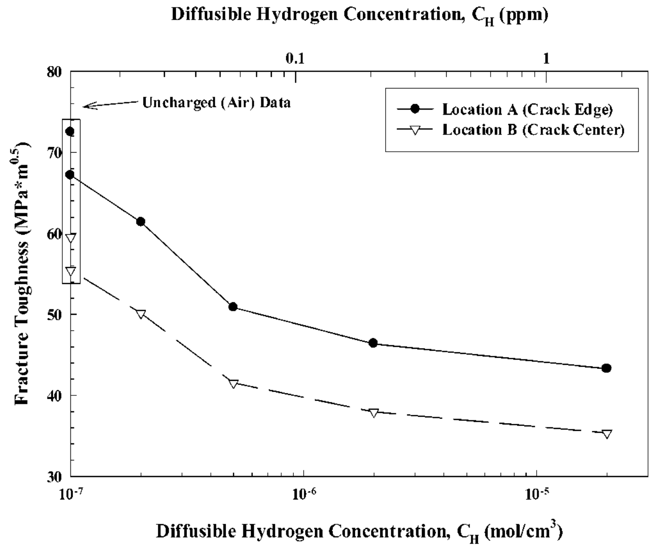

Fig. 14—Transverse fracture toughness as a function of diffusible hydrogen concentration for EDM notched and fatigue precracked tensile bars.

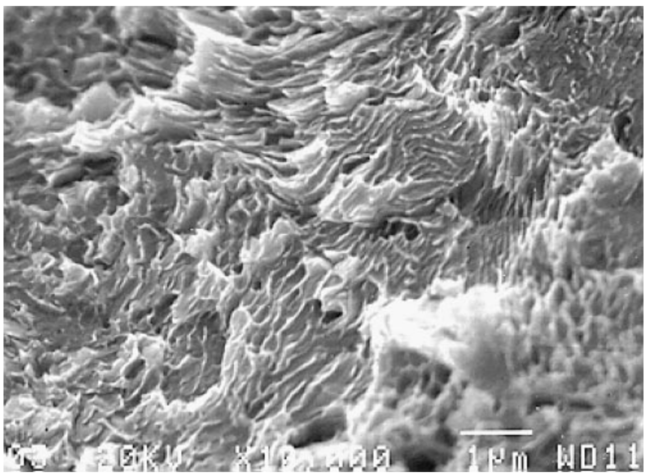

Fig. 12—High-magnification view of the lip region picture above from a specimen with moderate C_H (above C_{Hcrit}). Note the arrays of lamellar voids throughout the fracture surface, likely the result of the shear cracking process proposed by Miller and Smith.[13]

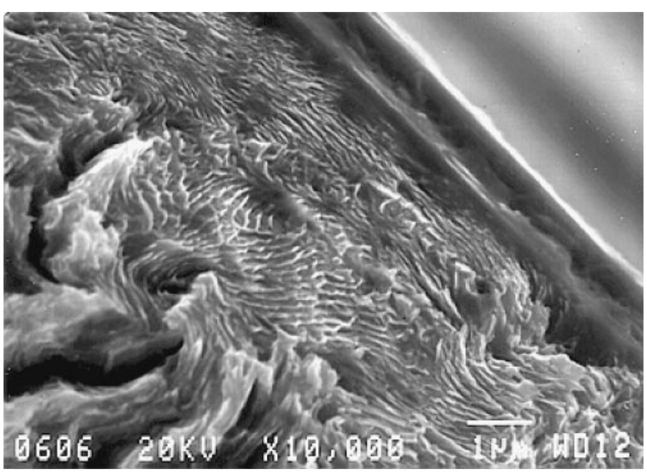

Fig. 13—High-magnification view of a typical lip region at high C_H, again illustrating the arrays of elongated voids, likely the result of shear cracking.

regions are still present (Figure 13). In addition, longitudinal splitting has become still more pronounced. Finally, the microscopically ductile region found at the notch root had less radial depth from the notch root, compared to that seen at lower C_H levels, in addition to possessing numerous small longitudinal cracks. Closer inspection of this region reveals extensive regions containing arrays of lamellar voids, as was observed at all other C_H levels (Figure 13). Little cleavage, inclusion-initiated or otherwise, is detected at this elevated C_H level.

6. *Fracture initiation from a sharp transverse crack—The determination of* K_{IHE}

The value of K_{IHE}, the stress intensity for transverse hydrogen crack initiation (*i.e.*, K_{IC} in the presence of dissolved hydrogen), was calculated as a function of C_H. The initial crack growth was within the same plane as the fatigue precrack (*i.e.*, mode I). As can be seen in Figure 14, a reduction of 15 pct in K_{IHE} is observed at a C_{Hcrit} of 2×10^{-7} mol/m^3, the C_H level below which embrittlement was not observed. This threshold C_H is comparable to that observed for the bluntly (2×10^{-7} mol/cm^3) and sharply (3.25×10^{-7} mol/cm^3) notched tensile bars. Although the prestressing steel is embrittled by hydrogen, the effect of C_H on the transverse K_{IHE} is not nearly as severe as for a quenched and tempered steel of equivalent yield strength and comparable C_H, where K_{IHE} values on the order of 20 MPa-m$^{1/2}$ are not uncommon.[17]

7. *Fractography for fatigue-precracked fracture-toughness specimens: Low* C_H *levels*

An overview of a fracture surface for a precracked specimen tested in air is presented in Figure 15. Along the edge of the fatigue precrack, numerous sites of mode I crack initiation are visible. These sites are composed of an array of lamellar voids (Figure 16) much like the small lip region in the notched tensile bars (Figures 10 through 13). Few regions of cleavage are observed. Beyond these initiation sites, the advancing crack rapidly turns parallel to the tensile axis, as illustrated in Figure 15. The crack surface parallel to the tensile axis indicates longitudinal splitting due to the

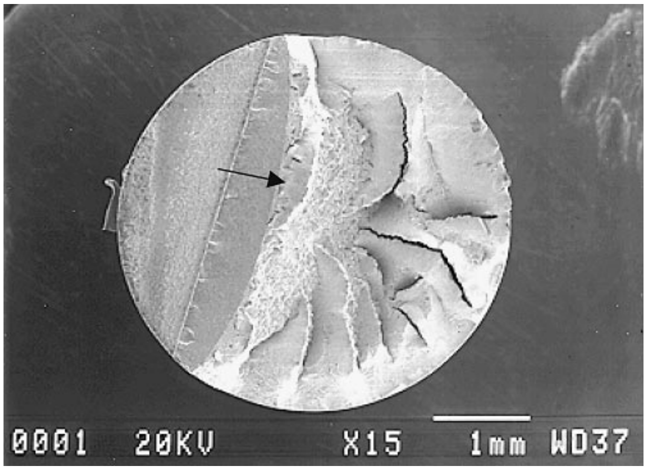

Fig. 15—Overview of the fracture surface for an uncharged, fatigue precracked ASTM A416, grade 270 prestressing tendon. The transverse chord-shaped EDM notch and fatigue precrack can be seen on left.

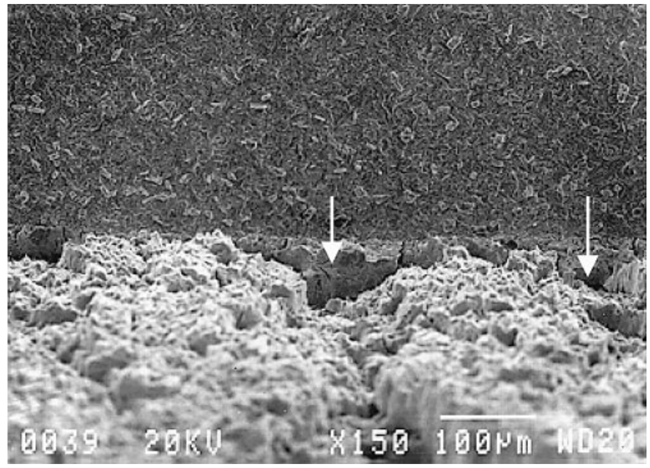

Fig. 17—Model I crack initiation sites (arrows) in front of the fatigue precrack for a fatigue precracked, hydrogen-charged (2×10^{-5} mol/cm^3) eutectoid prestressing steel tendon. Cracking is from top to bottom.

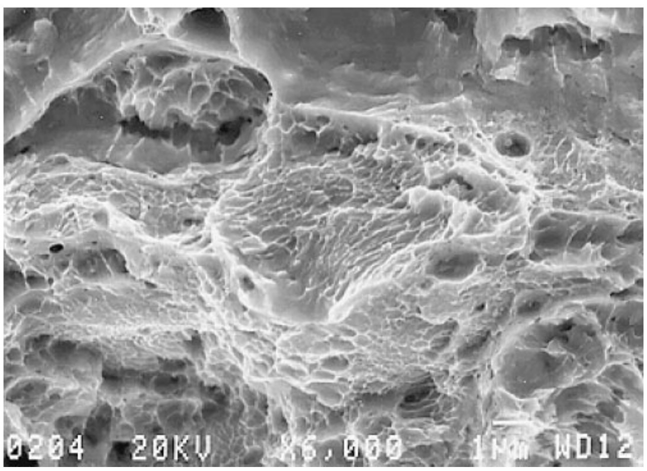

Fig. 16—High-magnification view of the initiation regions just to the right of the fatigue precrack in Fig. 15 (arrow). Note the array of lamellar voids throughout the fracture surface at the location of initiation, indicative of shear cracking, as proposed by Miller and Smith.[13]

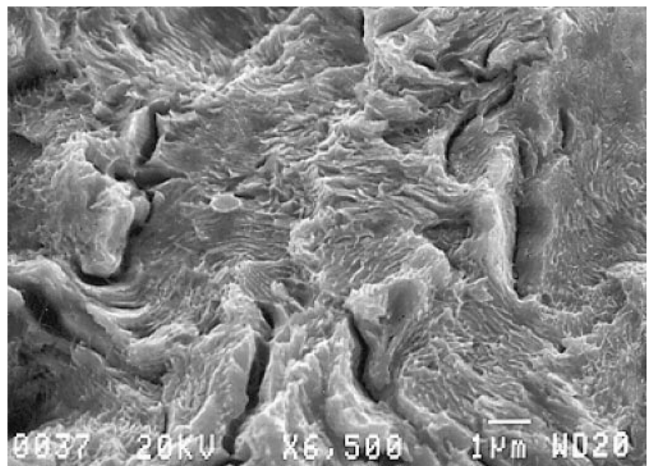

Fig. 18—High-magnification view of the fracture initiation sites indicated by the arrows in Fig. 17, illustrating numerous arrays of elongated voids, likely the result of shear cracking as proposed by Miller and Smith.[13]

highly anisotropic nature of the drawn pearlitic steel (*i.e.*, alignment of pearlite lamellae parallel to the wire axis). Beyond this region, the fracture surface becomes smooth and microscopically ductile in nature, the result of rapid ductile overload of the remaining ligaments between longitudinal splits.

8. *Moderate (2×10^{-6} mol/cm^3 or 0.254 ppm) and high (2×10^{-5} mol/cm^3 or 2.54 ppm)* C_H *levels*

There were numerous sites along the front of the fatigue precrack where a mode I crack was initiated, as observed for notched specimens. Microscopically, these sites were composed of lamellar voids, as seen in the lip regions for the notched tensile bars (Figures 10 through 13). These regions are likely shear cracks as proposed by Miller.[13] The fracture surface for the fatigue-precracked specimen tested at high C_H levels, possessed many of the microscopic features present in the notched specimens at lower C_H levels. These regions include the initiation regions in front of the fatigue precrack (Figure 17), which are composed of numerous lamellar voids (Figure 18) of dimensions near the interlamellar spacing of the pearlite. Beyond these initiation sites, the advancing crack turns roughly parallel to the tensile axis and appears similar to the tortuous region discussed previously. Beyond this tortuous region is a smooth, MVC region resulting from catastrophic shear overload of the remaining ligament. Cleavage was not observed.

B. *Hydrogen Partitioning Within the Prestressing Steel as a Function of the Uniform* C_H *Levels*

Figure 19 presents TDS spectra for a sample charged to a series of uniform C_H levels, then allowed to outgas at room temperature such that C_H had decayed to approximately zero. Samples were evaluated by TDS at thermal ramp rates of 2.5 °C/min, 5.1 °C/min, 7.6 °C/min, and 10.3 °C/min. Trap-state assignments are consistent with previous observations of trapping at dislocations, ferrite/cementite interfaces, and microvoids.[54–57] Note that an additional high-temperature trap state associated with oxide and MnS inclusions

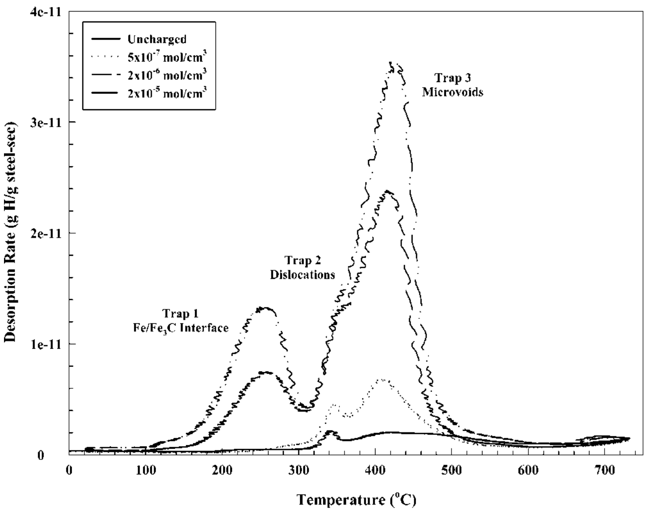

Fig. 19—Hydrogen desorption rate *vs* temperature as a function of initial diffusible hydrogen concentration (determined through electrochemical permeation experiments), illustrating the three discrete trap states within the prestressing steel. Ramp rate was 4.25 deg/min.

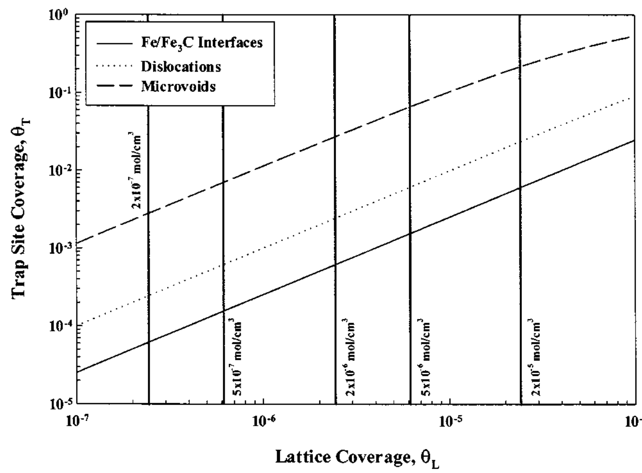

Fig. 20—Trap site coverage as a function of lattice coverage for fixed binding energies of 13.71 kJ/mol (Fe/Fe$_3$C interfaces), 17.12 kJ/mol (dislocations), and 23.16 kJ/mol (microvoids). Vertical lines indicate C_H values associated with testing in Figs. 6 through 19. Recall that $C_{Hcrit} > 3.25 \times 10^{-7}$ mol H/cm^3 in all tests.

Table I. Trap Site Identification and Desorption Peak Temperatures from TDS Experiments on Eutectoid Prestressing Steel

Trap Site	Slope	E_a (kJ/mol)	Likely Identification
1 (low T)	−2499.67	20.78	Fe/Fe$_3$C interface[54,55]
2 (medium T)	−2909.06	24.19	dislocations[54]
3 (high T)	−3635.44	30.23	microvoids[55]

Ramp Rate (Deg/Min)	Peak Temperature (°C) for Trap Sites		
	Fe/Fe$_3$C	Dislocations	Microvoids
2.5	204	300	359
5	252	345	424
7.5	282	390	461
10	315	434	493

Note: Calculation of E_b from E_a requires subtraction of the migration energy for ideal lattice diffusion (7.075 kJ/mol for iron[60]) as $E_a = E_b + E_m$.

was found in spring steels.[58] The temperature scan conducted here did not enable detection of these trap states by outgassing, due to high desorption energies (*e.g.*, 86 to 112 kJ/mol activation energies). There are at least three distinct trapping sites over the temperature range explored, as summarized in Table I. The value of E_b was determined from E_a using an E_m value of 7.075 kJ/mol.[60] It is interesting to note that prior plastic deformation increased the trapping associated with the Fe/Fe$_3$C interface and microvoids, without shifting the peak position. The anticipated coverage of each trap site for a given steady-state C_H and corresponding C_L level was determined. Equation [4] was used to determine trap coverage from interstitial-lattice coverage. The values of C_L and $C_L/N_L = \theta_L$ were determined from pre-existing steady-state permeation data[36–39] using Fick's first law and knowledge of the foil thickness ($D_L = 1.3 \times 10^{-5}$ cm^2/s for bcc iron[61]) and a tortuosity factor of 0.2 to account for the path through the eutectoid ferrite phase. Such a path-length correction factor was used to determine C_L for duplex stainless steel.[62] Figure 20 presents the trap coverage for the three identified trap states in the prestressing steel as a function of the lattice hydrogen coverage. As can be seen in the figure, the trap-site coverage for Fe/Fe$_3$C interfaces* increases from 1.6×10^{-4} at a C_H of 5×10^{-7} mol/cm^3 to 6.1×10^{-3} at a C_H of 2×10^{-5} mol/cm^3. The H coverage at dislocation traps also increases with C_H, rising from 6.1×10^4 to 2.4×10^{-2} over the same range of C_H. The coverage of the strongest trap site, corresponding to microvoids, increases from 7×10^{-3} to greater than 0.2 over the same range of C_H. Microvoids may be associated with the tips of fractured cementite lamellae, inclusion/steel interfacial cracks generated by cold working, or dislocation pileups. Trap coverages at high-binding-energy inclusions would likely also be very high. Also note that evidence of substantial trapping supports the notion that the total hydrogen concentration (*i.e.*, lattice + reversibly trapped + irreversibly trapped) is much greater than C_H. Therefore, threshold total hydrogen concentrations for embrittlement likely exceed a few weight parts per million.

*Although the lowest-energy site has been tentatively identified as Fe/Fe$_3$C interfaces from the literature, it is not clear whether the hydrogen is trapped at the interface or within the cementite at individual carbon atoms. Consider a $C_H = 3.1 \times 10^{-7}$ mol/cm^3, the coverage of the Fe/Fe$_3$C trap site is found to be 0.006. Based upon this coverage, if one hydrogen atom were trapped at each carbon atom within the cementite, there should be 1.024×10^{-4} mol H/cm^3 Fe. However, from the TDS spectra, only 5.885×10^{-7} mol H/cm^3 Fe are found at this trap site. As such, it is reasonable to assume that hydrogen is, in fact, trapped at the interface and not within the cementite lamellae.

IV. DISCUSSION

A. *Proposed Model for Hydrogen Embrittlement of Prestressing Steel*

Cracking in isotropic pearlitic steels is brittle in nature, with cleavage-crack initiation occurring either at interrupted shear cracks, formed by the mechanism proposed by Miller and Smith,[13] or fractured MnS inclusions.[15] Upon hydrogen charging, however, isotropic pearlitic structures are seen

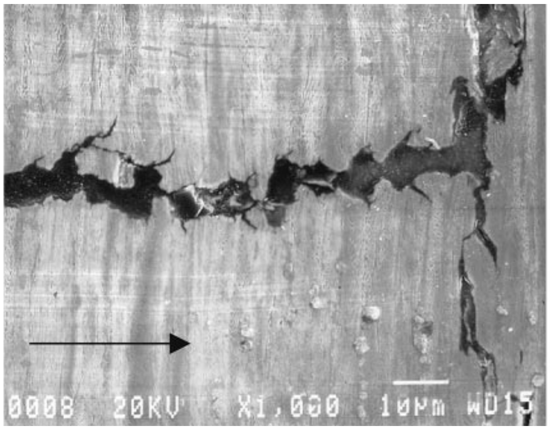

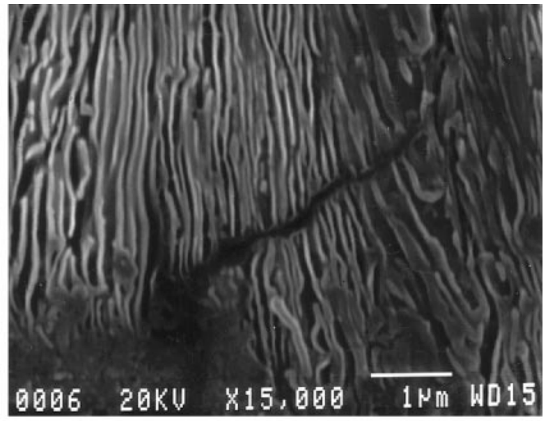

Fig. 21—Unetched and etched metallographic cross section of a transverse fatigue-precracked prestressing steel specimen (Fig. 5), illustrating t he shear cracking which occurs at approximately 45 deg. from the advancing horizontal fatigue precrack (arrow indicates direction of crack advance) as well as the change in direction of the advancing hydrogen crack to a direction parallel to the tensile axis (vertical).

to initiate cracks in a microscopically ductile fracture mode at lower stress intensities and to propagate cracks by brittle cleavage in mode I.[16,20–22,24,32] In cold-drawn steels, hydrogen promotes an increase in uniformly ductile, TTS fracture[16,20–22,24,32] and shear cracking of the pearlite lamellae.[13]

In this study, shear cracking of pearlite lamellae was observed to initiate at or near the surface of the transverse notch or edge of the transverse fatigue precrack at all C_H and constraint levels (Figures 10 through 13 and 16 through 18). These shear cracks were located where both the maximum shear stress, as well as the plastic strain, were maximized, but closer to the surface than the position of maximum longitudinal tensile stress or hydrostatic stress. Similarly. Lewandowski observed crack initiation closer to the notch root than the position of the maximum longitudinal stress in isotropic pearlitic microstructures.[15] Recall that the proposed shear-cracking process involves the formation of slip bands within the ferrite lamellae within a plane close to 45 deg from the tensile axis.[13] In prestressing steel with the $\langle 110 \rangle$ direction of ferrite lamellae oriented parallel to the wire axis, slip could occur along the $\langle 112 \rangle$ directions in $\{110\}$ ferrite planes that form an angle of 60 deg with the tensile axis. In such cases, the $\langle 112 \rangle$ directions will be oriented at angles of 30, 54.7, 73.2, and 90 deg from the tensile axis. Such slip, if localized enough to shear cementite lamellae, would crack such cementite lamellae and continue to localize slip in adjacent ferrite. Metallographic cross sectioning revealed such cracking,[15] which is illustrated in Figure 21. The tips of failed cementite lamellae subsequently act as void nuclei within the ferrite lamellae. Voids nucleated in this manner then grow within the ferrite lamellae and link up to form a macroscopic crack. Thus, the Miller process requires *tensile shear stresses* to fail the cementite lamellae, combined with a sufficiently large local plastic strain to promote void growth and coalescence through the ferrite.

Numerous investigators[63–69] have used stress-modified, critical-strain models for fracture conditions controlled by dimple rupture[69] or slip-band cracking.[68] In these models, fracture is defined when an applied local strain exceeds an intrinsic critical-failure strain ($\varepsilon^f_{\text{eff}}$) over a microstructurally significant distance (l^*), such as a multiple of the mean distance between microvoid-producing particles. These critical plastic-strain-controlled models of initiation fracture toughness attempt to couple three elements: (1) crack-tip stress and strain fields, which define the local applied crack-tip stresses and strains that drive fracture, (2) the stress-state–dependent fracture strain $\varepsilon^f_{\text{eff}}(\sigma_m/\sigma_{fl})$, and (3) a microstructural distance over which microvoid fracture initiates.[69] The predicted fracture-initiation toughness is equivalent to the applied-stress intensity at which the crack-tip plastic strain exceeds $\varepsilon^f_{\text{eff}}(\sigma_m/\sigma_{fl})$ over l^*, where σ_m is the mean stress, and σ_{fl} the flow stress. In this study, the finite-element–derived sharp- and blunt-notch maximum, $\varepsilon^f_{\text{eff}}$, is taken as a measure of the stress-state–dependent intrinsic fracture resistance of the material, as ductile shearing across pearlite colonies and void formation was observed at the position of the notch where the maximum $\varepsilon^f_{\text{eff}}$ is achieved. Notably, $\varepsilon^f_{\text{eff}}(\sigma_m/\sigma_{fl})$ has been defined locally at two constraint levels for a series of different C_H levels. Taking the derivation of Lee, Majno, and Asaro,[64] based on the Hutchinson, Rice and Rosengren (HRR) near-tip field and crack-tip blunting described by McMeeking, the following expression is obtained for transverse fracture toughness:

$$K_{IC} = 6\sqrt{E\sigma_y l^*\, \varepsilon^f_{\text{eff}}\left(\frac{\sigma_m}{\sigma_{fl}}\right)} \qquad [11]$$

In this expression, the value of 6 is a constant appropriate for this steel, based on its work-hardening coefficient of 0.114 (as calculated from the true stress–true strain curve), an integration constant which is weakly dependent on work hardening, an angular strain-field factor at a line angled at 45 deg from the crack equator, and $\nu = 0.3$.[64] $\varepsilon^f_{\text{eff}}(\sigma_m/\sigma_{fl})$ is the sole hydrogen-concentration-dependent input and is obtained from Eqs. [6] and [10] for the sharp and blunt notches, respectively. The value of E is 185 GPa, σ_y is 1696 MPa, while l^* is the sole adjustable parameter. The terms E, σ_y, and l^* are independent of C_H, which is reasonable, considering the low diffusible hydrogen concentrations present in the steel.

Figure 22 illustrates a comparison of the transverse fracture-initiation toughness estimated from Eq. [11] and the experimental toughness data using the K_I solutions for positions A and B. It is notable that a reasonable match is obtained between the ductile model of Eq. [11] and the actual results when l^* is fixed for all C_H values at a distance of 6 μm, equal to the pearlite colony size in this steel.

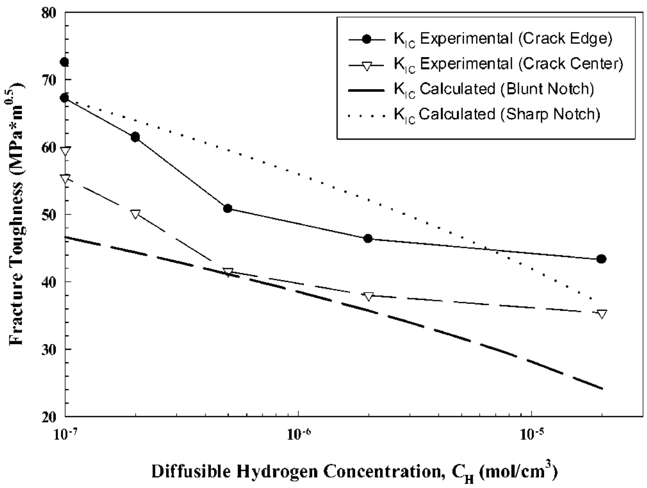

Fig. 22—Comparison of the predicted fracture toughness calculated from the model proposed in this study (Eq. [11]) to the experimental fracture toughness data obtained from hydrogen charged, precracked prestressing steel.

Numerous investigators have observed shear cracking across entire pearlite colonies.[5,13,15] Recall that ductile pearlite shearing was always observed at the notch root of notched specimens and below the fatigue precrack of fracture specimens (Figure 21). Furthermore, none of the fracture surfaces had the characteristic appearance of cleavage crack initiation from a particle, such as an MnS inclusion. Physically, this result suggests that when the applied crack-tip tensile strain exceeds a hydrogen-dependent value of $\varepsilon^f_{\text{eff}}(\sigma_m/\sigma_{fl})$ over a distance equal to the mean pearlite colony size, lamellar shearing occurs. Since $\varepsilon^f_{\text{eff}}(\sigma_m/\sigma_{fl})$ is lowered by hydrogen, l^* can be exceeded by an increasingly modest applied strain achieved at a lower remotely applied stress.

B. *Uncertainties in the Proposed Ductile-Fracture Model*

The proposed model is an oversimplification of the complex events occurring at the crack tip undergoing ductile microvoid nucleation, growth, and coalescence (MNGC). The concept of a critical fracture strain is readily accepted, but difficult to measure.[68] Tensile- and plane-strain ductilities may not be representative of these properties at a crack tip (*i.e.*, $\varepsilon^f_{\text{eff}}$ is dependent on (σ_m/σ_{fl}) and the constraint varies with distance ahead of the crack tip),[68,69,70] the damage mechanism may differ between a notch and crack tip,[64] crack-tip hydrogen concentrations may differ from C_H due to stress-field occlusion, and models of crack-tip strain fields may be inaccurate.[71,72,73] Given all these difficulties, it is interesting to note the general agreement between the model and the actual results (Figure 22). More rigorous fracture modeling must include either $\varepsilon^f_{\text{eff}}(\sigma_m/\sigma_{fl})$ measurements over a range of global-constraint levels so that the functional relationship between $\varepsilon^f_{\text{eff}}(\sigma_m/\sigma_{fl})$ and constraint can be obtained,[74] or involve direct determination of $\varepsilon^f_{\text{eff}}(\sigma_m/\sigma_{fl})$ from void-growth measurements at the crack tip.[68,75] By using the former approach, the presumed form of the $\varepsilon^f_{\text{eff}}(\sigma_m/\sigma_{fl})$ function $\{\varepsilon^f_{\text{eff}}(\sigma_m/\sigma_{fl}) = \alpha \exp(-\beta(\sigma_m/\sigma_{fl}))\}$ could be superimposed on a plot of applied crack-tip plastic strain *vs* distance from the crack tip.[74] Interception of these two plots leads to rigorous determination of the intrinsic fracture strain and the critical distance ahead of the crack tip, l^*. However, in this study, $\varepsilon^f_{\text{eff}}(\sigma_m/\sigma_{fl}) = \alpha \exp(-\beta(\sigma_m/\sigma_{fl}))$ would have to be characterized at each C_H value. If $\varepsilon^f_{\text{eff}}(\sigma_m/\sigma_{fl})$ is overestimated due to use of low-constraint notch data, then l^* is underestimated. In the present study, it is likely that the shape of the predicted K_I *vs* C_H curve is not accurately captured due to these complexities. It is worth noting that several factors may be roughly offsetting. Since void growth during ductile shearing occurs just below the notch, it is clearly beneath the position of maximum global triaxial tensile stress (*e.g.*, 10 μm from the notch root in Figure 13 *vs* the maximum global hydrostatic tensile stress at 80 μm). Therefore, the use of lower-constraint notch $\varepsilon^f_{\text{eff}}(\sigma_m/\sigma_{fl})$ data may be justified, and C_H should not be modified for stress-field occlusion. If these deductions are incorrect, then $\varepsilon^f_{\text{eff}}(\sigma_m/\sigma_{fl})$ is overestimated. In contrast, the larger at-risk volume of the notches, especially the blunt notch, may lead to a higher probability of encountering a worse flaw at a lower applied strain than when pearlite shearing occurs within the smaller at-risk volume of the crack tip. The value of $\varepsilon^f_{\text{eff}}(\sigma_m/\sigma_{fl})$ is then underestimated. Errors due to these factors may be roughly offsetting. In summary, although this simplified analysis gives insight into the crack-initiation phenomena, its shortcomings should be recognized.

C. *Longitudinal Splitting*

Once large shear cracks have been initiated from transverse notches, they propagate to an undefined microstructural defect oriented parallel to the tensile axis, which, in turn, triggers longitudinal cracking at an apparently low applied normal stress (albeit raised by the presence of the shear cracks and tensile-stress field triaxiality) in the transverse direction relative to the combined shear stress/normal stress required to initiate Miller shear cracking. Longitudinal splitting is the propagation of a brittle crack parallel to the drawing axis, as indicated by the brittle facets discussed previously and shown in Figure 21(a). Longitudinal splitting may occur along the boundary between adjacent pearlite colonies, along dislocation cells, or near prior-austenite grain boundaries, which are all elongated parallel to the wire axis as a result of the drawing process.[30] Thus, longitudinal splitting substitutes for the advancing shear crack by cracking along an extremely weakened interface in the highly aligned microstructure. This weakened interface may not be aligned favorably to a high normal stress until it is intersected by an advancing shear crack. Eventually, the shear stress in the remaining ligament promotes catastrophic ductile-shear overload of the remaining ligament or ligaments between longitudinal splits. The question arises as to whether splitting can occur prior to meeting the criteria for wholesale shear-crack formation from a transverse notch. Recall that cleavage-crack initiation in isotropic eutectoid steels requires the presence of microcracks either formed by pearlite shear cracking or inclusions. Ogawa reports that the critical C_H for hydrogen-induced cracking in hypoeutectoid steels is a direct function of the square of the inclusion length.[76] It is reasonable to hypothesize that a large-enough at-risk fracture volume presents the possibility of longitudinal splitting at low effective tensile stresses, either as a consequence of early shear cracking in an appropriately oriented, large pearlite colony at a particularly large inclusion or inclusion density within the volume of the notch, or in poor-quality steels containing pre-existing longitudinal splits.

D. *Proposed Hydrogen Embrittlement Mechanism Associated with Shear Cracking*

Based upon the increase in shear cracking and the reduction of both the fracture-initiation strain and transverse-stress intensity with C_H, it seems likely that hydrogen either (1) reduces the shear or tensile fracture stress of the cementite lamellae, which, in turn, act as void nuclei; (2) promotes localization of deformation to produce more intense shear bands in the ferrite, which raises the applied shear stress on the cementite by a Stroh mechanism;[77] or (3) assists in the void growth and linkup stage of the shear-cracking process.[13]

In both isotropic and cold-worked pearlitic steels, hydrogen charging results in two types of ductile fracture modes (defined as Miller shear cracking and TTS). This increase in ductile nature is to be expected when the effects of hydrogen on steels such as these are considered. Oriani and Josephic[78] found that hydrogen reduced the lattice-cohesion strength for pearlitic 1045 steel (*i.e.*, decohesion occurs at a lower applied stress with increasing C_H). As a result, void nucleation at ferrite/cementite interfaces, followed by growth within the ferrite, occurs more readily. Thus, more numerous (due to enhanced void nucleation), larger (due to enhanced void growth) voids are formed for a given macroscopic strain, leading to failure at lower macroscopic strains with increased C_H. Cialone and Asaro[79] found that void nucleation at Fe_3C interfaces was enhanced by hydrogen for spheroidized 1090 steel, as were the latter stages of void growth and coalescence. They speculated that the mechanism was that a high hydrogen pressure was achieved within microvoids, which, in turn, aided the remotely applied stress, but were unable to conclusively prove their theory. Garber *et al.*[80] identified that hydrogen-assisted void linkup, but it had little effect on void nucleation or growth. Onyewuenyi and Hirth[81] studied spheroidized 1090 steel and found that increased hydrogen resulted in increased dislocation injection from second-phase particles within the ferritic matrix, and that hydrogen enhanced the mobility of screw dislocations. To summarize all of these literature findings, hydrogen may stimulate plastic flow through enhanced dislocation generation, promote slip localization for a given amount of strain, enhance void nucleation, and accelerate void growth. As a result, ductile failure may be achieved at lower global applied tensile strains and, thus, lower remotely applied stresses. From the literature, recall that the α-Fe/Fe_3C interface is a site of enhanced void nucleation, and hydrogen must accumulate there to promote void nucleation of new voids.[79]

Recall the TDS results of the cold-drawn steels presented previously. The hydrogen coverage (θ_T) of trap sites identified as α-Fe/Fe_3C interfaces and microvoids increases as C_L and C_H increase. Figures 23 and 24 present the fracture-initiation strain as a function of the hydrogen-trap coverage at α-Fe/Fe_3C interfaces and microvoids, respectively. It can be seen that although the global C_H (and corresponding lattice-site coverages, θ_L) are low, the coverage at microvoids approaches 0.1 under conditions where embrittlement is

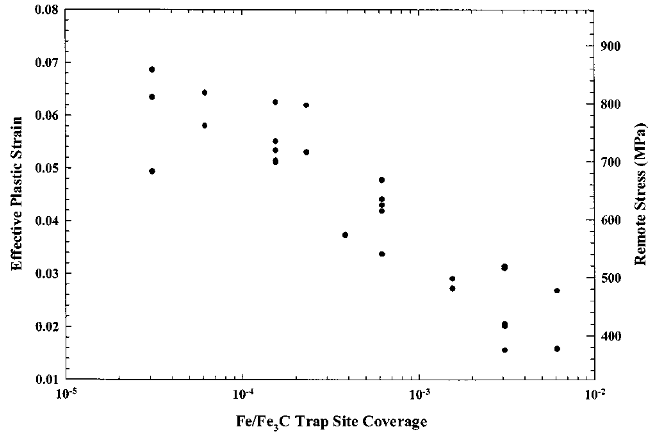

Fig. 23—Effective plastic strain at notch equator and remote stress at failure as a function of Fe/Fe_3C trap site coverage for eutectoid prestressing steel.

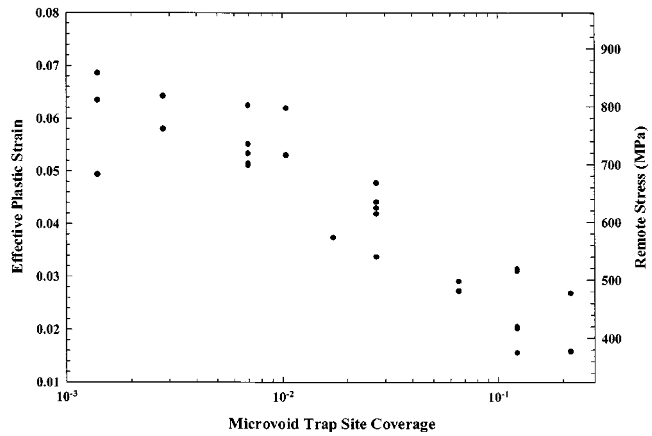

Fig. 24—Effective plastic strain at notch equator and remote specimen stress at failure as a function of microvoid trap site coverage for eutectoid prestressing steel.

severe. The critical condition for embrittlement of the prestressing steel occurred (the conditions for the onset of reduction of the remote stress and local strain required to nucleate a crack) at trap-site coverages of approximately 6.2×10^{-5} for Fe/Fe_3C interfaces and 2.8×10^{-3} for microvoids. The corresponding critical diffusible hydrogen concentration C_{Hcrit} is approximately 2.45×10^{-7} mol/cm^3. Given the potency of hydrogen as an embrittling agent, these results implicate microvoids as the critical trap site, because the interface coverage appears to be too low at Fe/Fe_3C interfaces to produce much damage. Damage was most severe when the microvoid trap coverage approached or exceeded 0.1. Concerning the micromechanisms of crack nucleation, such trapped hydrogen may enhance both cementite shearing and void nucleation at ferrite/cementite interfaces, but appears more likely to enhance void growth and propagation through the ferrite lamellae. A shear crack is nucleated and grown to critical dimensions at a lower remotely applied stress (and, hence, strain) when C_H and θ_T are increased.

V. CONCLUSIONS

1. A threshold C_{Hcrit} (2×10^{-7} mol/cm^3) was obtained for reduction of the axial fracture-initiation stress of a bluntly

notched steel. A universal relationship between a prestressing steel's absorbed C_H and the local fracture-initiation strain was established. The relationship is of the form $\varepsilon^f_{eff} = \varepsilon_{air} - \alpha \log (C_H/C_{Hcrit})$, where ε^f_{eff} is the local fracture-initiation stress, C_H is the diffusible hydrogen concentration (*i.e.*, lattice + weakly trapped), and C_{Hcrit} is the diffusible hydrogen concentration below which hydrogen has no influence on fracture initiation.

2. Three discrete hydrogen trap sites exist within the prestressing steel microstructure, identified at α-Fe/Fe_3C interfaces, microvoids, and dislocations. Hydrogen trapping at inclusions also may occur. The concentration trapped at the former sites has been demonstrated through trap-binding-energy analysis to increase significantly with increasing C_H and C_L.
3. Transverse crack initiation within cold-drawn, fully pearlitic steels is seen to take place near the notch root or tip of the fatigue precrack, where the combination of shear stress and effective strain are maximized. Once such a crack forms, it continues to grow until reaching a microstructural defect oriented parallel to the wire axis, such as a pearlite subcolony interface, triggering longitudinal splitting.
4. Transverse crack initiation within the heavily cold-worked pearlitic steels utilized as prestressing tendons occurs through the formation of shear cracks[13] across pearlite colonies, which, in turn, trigger longitudinal splitting, followed by ductile overload of the remaining ligament of the tensile bar. This process is assisted by hydrogen, which either reduces the cohesive strength of the Fe/Fe_3C interface, localizes slip to more readily enable shearing of Fe_3C, or assists void growth and coalescence, consistent with hydrogen trapping at these sites. The end result is that wholesale shear cracking across pearlite colonies is achieved at lower applied remote (*i.e.*, global) strains.
5. A stress-modified, critical-strain model of fracture-initiation toughness proposed in the literature was adapted to the case of hydrogen-controlled pearlite shear cracking occurring by MNGC in shear bands across pearlite colonies. Good agreement with actual fracture-initiation-toughness values was obtained when the sole adjustable parameter of the model, l*, was set to the dimension of shearable pearlite colonies. The effect of hydrogen was incorporated through the relationship between ε^f_{eff} and C_H.

REFERENCES

1. R.N. Parkins, M. Elices, V. Sanchez-Galvez, and L. Caballero: *Corr. Sci.*, 1982, vol. 22 (5), pp. 379-405.
2. W.H. Hartt, C.C. Kumria, and R.J. Kessler: *Corrosion*, 1993, vol. 49 (5), pp. 377-85.
3. W.H. Hartt, O. Chaix, R.J. Kessler, and R. Powers: *Corrosion 94*, NACE, Houston, TX, 1994, paper no. 291.
4. J. Embury and R. Fisher: *Acta Metall.*, 1966, vol. 14 (2), pp. 147-59.
5. V. Chandhok, A. Kasak, and J.P. Hirth: *Trans. ASM*, 1966, vol. 59, pp. 288-301.
6. D.A. Porter, K.E. Easterling, and G.D.W. Smith: *Acta Metall.*, 1978, vol. 26, pp. 1405-22.
7. J.J. Lewandowski and A.W. Thompson: *Metall. Trans. A*, 1986, vol. 17A, pp. 461-72.
8. J.J. Lewandowski and A.W. Thompson: *Metall. Trans. A*, 1986, vol. 17A, pp. 1769-86.
9. J.J. Pepe: *Metall. Trans.*, 1973, vol. 4, pp. 2455-60.
10. A. Athanassiadis, J. Boissenot, P. Brevet, D. Francois, and A. Raharinaivo: *Int. J. Fract.*, 1981, vol. 17 (6), pp. 553-66.
11. K. McGuinn and J.R. Griffiths: *Br. Corr. J.*, 1977, vol. 12 (3), pp. 152-57.
12. K. McGuinn and M. Elices: *Br. Corr. J.*, 1981, vol. 16 (3), pp. 132-39.
13. L.E. Miller and G.C. Smith: *J. Iron Steel Inst.*, 1970, vol. 208 (11), pp. 998-1005.
14. Y.J. Park and I.M. Bernstein: *Metall. Trans. A*, 1979, vol. 10A, pp. 1653-64.
15. J.J. Lewandowski and A.W. Thompson: *Acta Metall.*, 1987, vol. 35 (7), pp. 1453-62.
16. J. Toribio and A. Lancha: *J. of Materials Science*, 1996, vol. 31(22), pp. 6015-24.
17. R.P. Gangloff: *Corrosion Prevention and Control: 33rd Sagamore Army Materials Research Conf.*, Burlington, VT, U.S. Army Materials Technology Laboratory, Watertown, MA, 1986, p. 64-111.
18. B. Marandet: in *Stress Corrosion Cracking and Hydrogen Embrittlement of Iron Base Alloys*, R. Staehle, ed. *National Association of Corrosion Engineers, (NACE-5)*, Houston, TX, 1977, pp. 774-87.
19. A.W. Thompson: *Mater. Sci. Technol.*, 1985, vol. 1 (9), pp. 711-18.
20. J. Toribio, A.M. Lancha, and M. Elices: *Corrosion*, 1991, vol. 47 (10), pp. 781-91.
21. J. Toribio, A.M. Lancha, and M. Elices: *Mater. Sci. Eng. A*, 1991, vol. 145, pp. 167-77.
22. J. Toribio and A.M. Lancha: *Mater. Struct.*, 1993, vol. 26 (1), pp. 30-37.
23. A. Thompson and J. Chesnutt: *Metall. Trans. A*, 1979, vol. 10A, pp. 1193-96.
24. J. Toribio: *J. Mater. Sci.*, 1993, vol. 28, pp. 2289-98.
25. N. Sarafianos: *J. Mater. Sci. Lett.*, 1989, pp. 1486-88.
26. D. Langstaff, G. Meyrick, and J.P. Hirth: *Corrosion*, 1981, vol. 37 (8), pp. 429-37.
27. H.J. Townsend: *Corrosion*, 1972, vol. 28 (2), pp. 39-46.
28. S.M. Price: *Int. Congr. on Metallic Corr.*, 1984, vol. 2, pp. 262-69.
29. B.W. Cherry and S.M. Price: *Corr. Sci.*, 1980, vol. 20, pp. 1163-83.
30. W. Hosford: *Trans. TMS-AIME*, 1964, vol. 230 (2), pp. 12-15.
31. F.P.L. Kavishe and T.J. Baker: *Mater. Sci. Technol.*, 1986, vol. 2 (6), pp. 583-88.
32. J. Toribio, A.M. Lancha, and M. Elices: *Metall. Trans. A*, 1992, vol. 23A, pp. 1573-84.
33. J.M. Hyzak and I.M. Bernstein: *Metall. Trans. A*, 1976, vol. 7A, pp. 1217-24.
34. M.C. Alonso, R.P.M. Procter *et al.*: *Corr. Sci.*, 1993, vol. 34 (6), pp. 961-73.
35. K. McGuinn and J.R. Griffiths: *Br. Corr. J.*, 1997, vol. 12 (3), pp. 152-57.
36. D.G. Enos, A.J. Williams, Jr., and J.R. Scully: *Corrosion 96*, 1996, paper no. 307.
37. D.G. Enos, A.J. Williams, Jr., G.G. Clemeña, and J.R. Scully: *Corrosion 97*, 1997, paper no. 241.
38. D.G. Enos, A.J. Williams, Jr., and J.R. Scully: *Corrosion*, 1997, vol. 53 (11), pp. 891-908.
39. D.G. Enos, A.J. Williams, Jr., G.G. Clemeña, and J.R. Scully: *Corrosion*, 1998, vol. 54 (5), pp. 389-402.
40. M.A. Gaudett and J.R. Scully: *Metall. Mater. Trans. A*, 1999, vol. 30A, pp. 65-79.
41. M. Caspers, C. Mattheck *et al.*: *Z. Werkstofftech.*, 1986, vol. 17, pp. 327-33.
42. M. Caspers and C. Mattheck: *Fatigue Fract. Eng. Mater. Struct.*, 1987, vol. 9 (5), pp. 329-41.
43. W. Blackburn: *Eng. Fract. Mech.*, 1976, vol. 8, pp. 731-36.
44. A. Carpinteri: *Eng. Fract. Mech.*, 1992, vol. 42 (6), pp. 1035-40.
45. A. Levan and J. Royer: *Int. J. Fract.*, 1993, vol. 61, pp. 71-99.
46. E. Si: *Eng. Fract. Mech.*, 1990, vol. 37 (4), pp. 805-12.
47. I. Raju and J. Newman: *Fract. Mech.: 17th Volume*, J. Underwood, R. Chait, and C. Smith, ASTM STP 905, ASTM, Philadelphia, PA, 1986, pp. 789-805.
48. R.D. Goolsby and L.K. Austin: *7th Int. Conf. on Fracture*, K. Salama, ed., Pergamon Press, Elmsford, NY, 1989, vol. 4, pp. 2423-35.
49. R.S. Lillard and J.R. Scully: *Corrosion*, 1996, vol. 52 (2), pp. 125-37.
50. P.A. Klein, R.A. Hays, P.J. Moran, and J.R. Scully: *ASTM STP 1210: Slow Strain Rate Testing for the Evaluation of Environmentally Induced Cracking*, R.D. Kane, ed., ASTM, Philadelphia, PA, 1993, pp. 202-22.
51. M.A.V. Devanathan and Z. Stachurski: *Proc. R. Soc. (London)*, 1962, vol. 270A, pp. 90-102.

52. M.A.V. Devanathan and Z. Stachurski: *J. Electrochem. Soc.*, 1964, vol. 111 (5), pp. 619-23.
53. S.W. Smith and J.R. Scully: *Metall. Mater. Trans. A*, 2000, vol. 31A, pp. 179-93.
54. W.Y. Choo and J.Y. Lee: *Metall. Trans. A*, 1982, vol. 13A, pp. 135-40.
55. G.W. Hong and J.Y. Lee: *Mater. Sci. Eng.*, 1983, vol. 61, pp. 219-25.
56. J.Y. Lee, J.L. Lee, and Y.W. Choo: in *Current Solutions to Hydrogen Problems in Steels*. C.G. Interrante and G.M. Pressouyre, eds., ASM, Metals Park, OH, 1984, pp. 423-27.
57. H.G. Lee and J.-Y. Lee: *Acta Metall.*, 1984, vol. 32 (1), pp. 131-36.
58. K. Lee, J.-Y. Lee, and D.R. Kim: *Mater. Sci. Eng.*, 1984, vol. 67, pp. 213-20.
59. K. Yamakawa: *Int. Congr. on Metallic Corrosion*, 1984, vol. 2, pp. 254-61.
60. N.R. Quick and H.H. Johnson: *Acta Metall.*, 1978, vol. 26, pp. 903-07.
61. A.J. Kumnick and H.H. Johnson: *Metall. Trans.*, 1974, vol. 5, pp. 1199-1206.
62. A.J. Griffiths and A. Turnbull: *Corrosion*, 2001, vol. 57 (2), pp. 165-74.
63. R.O. Ritchie, W.L. Server, and R.A. Wullaert: *Metall. Trans. A*, 1979, vol. 10A, p. 1557.
64. S. Lee, L. Majno, and R.J. Asaro: *Metall. Mater. Trans. A*, 1995, vol. 16A, pp. 1633-48.
65. N.R. Moody, R.E. Stolz, and M.W. Perra: *Metall. Trans. A*, 1987, vol. 18A, pp. 1469-82.
66. R.O. Ritchie and A.W. Thompson: *Metall. Trans. A*, 1985, vol. 16A, pp. 233-48.
67. W.M. Garrison and N.R. Moody: *J. Phys. Chem. Solids*, 1987, vol. 48, pp. 1035-74.
68. N.R. Moody, S.L. Robinson, and M.W. Perra: *Eng. Fract. Mech.*, 1991, vol. 39 (6), pp. 941-54.
69. M.J. Haynes and R.P. Gangloff: *Metall. Trans. A*, 1997, vol. 28A, pp. 1815-29.
70. J.W. Hancock and A.C. MacKenzie: *J. Mech. Phys. Solids*, 1976, vol. 24, pp. 147-69.
71. J.W. Hutchinson: *J. Mech. Phys. Solids*, 1968, vol. 25, p. 13.
72. J.R. Rice and G.F. Rosengren: *J. Mech. Phys. Solids*, 1968, vol. 16, p. 1.
73. R.M. McMeeking: *J. Mech. Phys. Solids*, 1977, vol. 25, p. 357.
74. M.J. Haynes, B.P. Somerday, C.L. Lach, and R.P. Gangloff: in *Elevated Temperature Effects on Fatigue and Fracture*, R.S. Piascik, R.P. Gangloff, and A. Saxena, eds., ASTM STP 1297, ASTM, Philadelphia, PA, 1997, pp. 165-90.
75. F.A. McClintock: *J. Appl. Mech. Ser.*, 1986, vol. E35, pp. 363-71.
76. H. Ogawa and T. Hara: *13th Int. Corrosion Congr.*, Melbourne, Australia, ACA Inc., Clayton, Australia, 1996, paper no. 218.
77. A. Stroh: *Proc. R. Soc. London*, 1954, vol. 223, pp. 404-14.
78. R. Oriani and P. Josephic: *Acta Metall.*, 1979, vol. 27, pp. 997-1005.
79. H. Cialone and R. Asaro: *Metall. Trans. A*, 1979, vol. 10A, pp. 367-75.
80. R. Garber, I. Bernstein, and A.W. Thompson: *Metall. Trans. A*, 1981, vol. 12A, pp. 225-34.
81. O.A. Onyewuenyi and J.P. Hirth: *Scripta Metall.*, 1981, vol. 15 (1), pp. 113-18.